

Three universality classes for reaction fronts in disordered flows

S  verine Atis,¹ Awadhesh Kumar Dubey,¹ Dominique Salin,¹
Laurent Talon,¹ Pierre Le Doussal,² and Kay J  rg Wiese²

¹*FAST, CNRS, UPSud, UPMC, UMR 7608, Batiment 502, Campus Universitaire, 91405 Orsay, France.*
²*CNRS-Laboratoire de Physique Th  orique de l'  cole Normale Sup  rieure, 24 rue Lhomond, 75005 Paris, France.*

Self-sustained reaction fronts in a disordered medium subject to an external flow display self-affine roughening, pinning and depinning transitions. We measure spatial and temporal fluctuations of the front in 1 + 1 dimensions, controlled by a single parameter, the mean flow velocity. Three distinct universality classes are observed, consistent with the Kardar-Parisi-Zhang (KPZ) class for fast advancing or receding fronts, the quenched KPZ class (positive-qKPZ) when the mean flow approximately cancels the reaction rate, and the negative-qKPZ class for slowly receding fronts. Both quenched KPZ classes exhibit distinct depinning transitions, in agreement with the theory.

PACS numbers:

Growing interfaces are ubiquitous in nature, and appear in situations as different as proliferation of bacterial colonies [1], solidification [2], deposition of atoms on a surface [3, 4], liquid interfaces in porous media [5–7] or crack propagation in heterogenous materials [8, 9]. These systems have in common that they are driven out of equilibrium, and form scale-free structures. Identifying the subsequent universality classes is an important goal in order to understand the emergence of these scaling laws.

Autocatalytic reaction fronts propagating in the heterogenous flow field of a porous medium [4, 8] provide an example with a rich dynamics. In the absence of an externally imposed flow, the chemical reaction produces traveling waves with velocity V_0 inside the medium. An additional flow modifies this behavior according to its strength and orientation as compared to the chemical front velocity. The fronts become rough and can propagate either downstream or upstream at constant velocity, or remain frozen over a range of counter-flow rates, delimited by two distinct depinning transitions. Until now, the universal behavior of reaction fronts in disordered flows has not been characterized. In the present letter, using both experimental and numerical approaches, we investigate the spatial and temporal scaling properties of this growing interface the whole range of the flow forcing parameter F . We show that this is a well-controlled system encompassing several universality classes.

Two important classes predicted by the theory are:

- (i) non-linear stochastic growth governed by the (thermal) Kardar-Parisi-Zhang (KPZ) equation,
- (ii) growth where both the non-linearity and quenched disorder are present, described by the quenched KPZ (qKPZ) equation. It divides into two subclasses, positive qKPZ and negative qKPZ, depending on the sign of the non-linearity λ . Indeed, the qKPZ equation can be justified, as shown below, from the so-called eikonal approximation, valid in the thin reaction-front limit.

Finding unambiguous experimental realizations has been difficult, in part because of long-range effects, quenched disorder and a mixing of (i) and (ii) [1, 13–

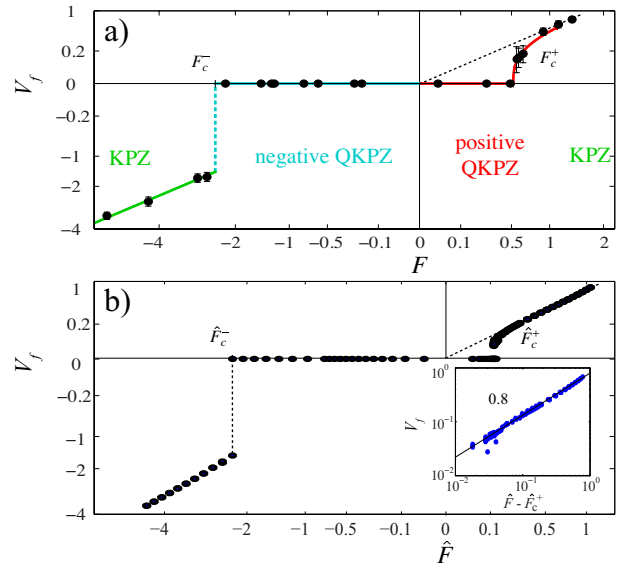


Figure 1: Front velocity V_f versus the applied force F (resp. \hat{F}), in adverse flow configuration. a) experiments (black dots with error bars). b) numerics (blue circles). Dashed lines are linear extrapolation of the advancing branch. To put all data on one plot, we rescaled the axes according to $F \rightarrow F/|F|^{1/2}$, $v \rightarrow v/|v|^{1/2}$. Insert: Log-Log plot of the front velocity versus $\hat{F} - \hat{F}_{c+}$. The continuous line corresponds to $v(\hat{F}) \propto (\hat{F} - \hat{F}_{c+})^{0.8 \pm 0.05}$

15]. Recently, remarkable experiments on turbulent liquid crystals (see [16] for a review) made a precise contact with the theory of the KPZ class which experienced a revolution of its own [17]. Some experiments also studied the (positive) qKPZ class [5, 18] and both KPZ and qKPZ classes were observed in evaporating colloidal suspensions [15]. Remarkably, in the present system, by tuning a *single* parameter F , one can observe *all three classes*.

The KPZ equation [19] was proposed as a generic

model for an interface growing along its local normal,

$$\frac{\partial h(x,t)}{\partial t} = \nu \nabla^2 h(x,t) + \frac{\lambda}{2} [\nabla h(x,t)]^2 + \eta(x,t) + f. \quad (1)$$

The height $h(x,t)$ of the interface is along the vertical axis, ν an effective stiffness due to diffusion, λ the non-linearity, and $\eta(x,t)$ a Gaussian white noise with correlations $\overline{\eta(x,t)} = 0$ and $\overline{\eta(x,t)\eta(x',t')} = 2D\delta(x-x')\delta(t-t')$. f is a constant applied force, and up to a shift, proportional to the experimental applied force F as shown below. The surface can be characterized by two scaling exponents, the roughness α , and the growth exponent β , defined via $[\overline{h(x,t) - h(x',t)}]^2 \sim |x - x'|^{2\alpha}$ and $[\overline{h(x,t) - h(x,t')}]^2 \sim |t - t'|^{2\beta}$. In $d = 1 + 1$ dimensions, the exponents are $\alpha_{\text{KPZ}} = 1/2$ and $\beta_{\text{KPZ}} = 1/3$ [19]. In a heterogeneous medium, the “noise” acquires a static *quenched* component, described by the qKPZ equation [20]:

$$\frac{\partial h(x,t)}{\partial t} = \nu \nabla^2 h(x,t) + \frac{\lambda}{2} [\nabla h(x,t)]^2 + \bar{\eta}(x, h(x,t)) + f. \quad (2)$$

The case $\lambda = 0$ models a number of systems, and is a distinct universality class (quenched Edwards-Wilkinson) [21] but does not seem to be relevant here (it predicts $\beta \approx 0.87$ and $\alpha > 1$).

In the KPZ equation (1) one can eliminate the driving term by the transformation $h(x,t) = ft + \tilde{h}(x,t)$. Changing then $\tilde{h}(x,t) \rightarrow -\tilde{h}(x,t)$ reverses the sign of the non-linear term λ , which is thus unimportant. By contrast, the qKPZ equation (2) does not allow for the change $h(x,t) = ft + \tilde{h}(x,t)$ since the term $\bar{\eta}(x, h(x,t))$ is not invariant. The driving force f is thus a new parameter of the problem, and its sign (relative to the sign of λ) matters: If the disorder is statistically invariant by parity, i.e. if $\bar{\eta}(x, -h)$ has the same properties as $\bar{\eta}(x, h)$, Eq. (2) is invariant under $f \rightarrow -f$, $h(x,t) \rightarrow -h(x,t)$, and $\lambda \rightarrow -\lambda$. Hence there are two distinct situations: Positive qKPZ when λ and f have the same sign, and negative qKPZ when they have opposite signs.

It is important to recall that in the moving phase qKPZ (of either sign) crosses over to KPZ at large scales. This is easily seen e.g. in the limit of large mean interface velocity $v = \partial_t \overline{h(x,t)}$: Consider Eq. (2) with white noise $\bar{\eta}(x, h)\bar{\eta}(x', h') = 2\bar{D}\delta(x-x')\delta(h-h')$ and perform the change $h(x,t) \rightarrow vt + \tilde{h}(x,t)$. The disorder then becomes

$$\bar{\eta}(x, vt + \tilde{h}(x,t)) \approx \bar{\eta}(x, vt), \quad (3)$$

i.e. the same noise as in the KPZ equation (1), identifying $D = \bar{D}/v$. As v is decreased, the crossover from qKPZ at short scales to KPZ occurs at larger and larger scales.

The positive qKPZ equation exhibits a depinning transition [20, 22] which is well characterized in $d = 1 + 1$. The mean interface velocity vanishes below a threshold $f < f_c^+$; for $f > f_c^+$ the interface moves with velocity $v \sim (f - f_c^+)^\theta$. At f_c the pinned interface outlines a

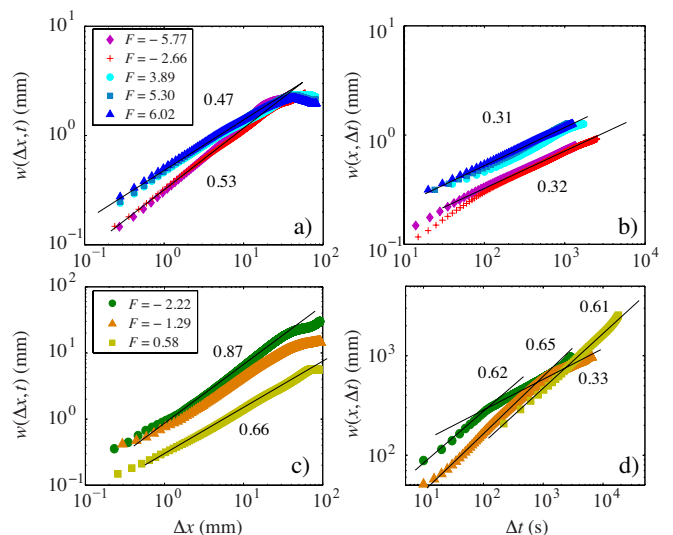


Figure 2: Height fluctuations of the front. Left column: roughness $w(\Delta x, t)$ and right column: temporal fluctuations $w(x, \Delta t)$. (a) and (b) for $|F| > 2.5$; (c) and (d) for $|F| < 2.5$.

transversal path on a directed percolation (DP) cluster [5, 18, 23] characterized by a roughness $\alpha_{\text{DP}} \simeq 0.63$, and a growth exponent $\beta_{\text{DP}} \simeq 0.63$. As discussed above the quenched nature of the noise is relevant only when f is close to its critical value.

The predictions for the negative qKPZ class are quite different [24]. In the pinned phase, $\lambda > 0$ and negative $f > f_c^-$, the interface forms sawtooth configurations (see Fig. 4, bottom) with alternating non-zero local average slopes $|\nabla h|$ which help the system to remain pinned. As f is decreased, the sawtooth slopes increase, until there are discontinuous jumps at f_c^- of both the average slope (back to zero) and the velocity v , well evident in our experiment, see Fig. 1 a). The transitory dynamics inside the pinned phase is similar to positive qKPZ [25], and the depinning near the jump was analyzed via a mapping to the first layer PNG model [6], a close cousin of KPZ.

Our experiments are made with the Iodate Arsenous Acid reaction, autocatalytic in iodide with the arsenous acid in excess [27, 28]. Resulting from the balance between the molecular diffusion D_m and the reaction rate $\bar{\alpha}$, this system develops a traveling reaction front, which propagates with a constant velocity $V_\chi = \sqrt{D_m \bar{\alpha}/2}$, and a stationary concentration profile of width $l_\chi = D_m/V_\chi$. Its position is visualized with polyvinyl alcohol colored by transient iodine production during the reaction [29]. The disordered flow is generated with a 50% mixture of 1.5 and 2 mm diameters packed glass beads inside a transparent ($300 \times 100 \times 4 \text{ mm}^3$) rectangular cell. Once filled with reactant solution, a range of injectors at the top of the cell can either suck out or inject the fluid parallel to the vertical. The chemical reaction is initiated at the bottom of the cell and forms initially a flat horizontal

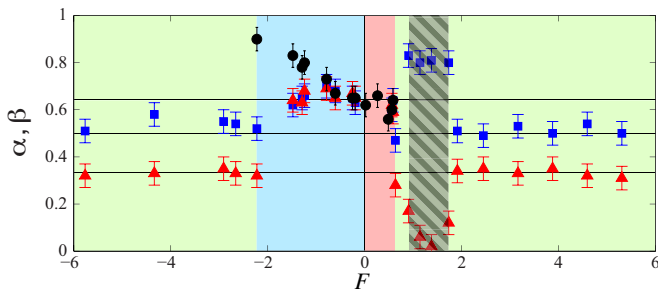


Figure 3: Experimental exponents versus F . Blue squares, roughness α and red triangles, growth exponent β for moving fronts. Black circles, roughness of the pinned fronts. Hatched region corresponds to weak noise when $\bar{U} \rightarrow 0$.

front. In the absence of the flow, the front propagates upwards at the chemical velocity $V_\chi \simeq 11.2 \mu\text{m/s}$ and width $l_\chi \simeq 200 \mu\text{m}$; once the desired vertical position is reached, the hydrodynamic flow is switched on.

The flow is characterized by its mean velocity \bar{U} and, as a control parameter, we define $F = \frac{\bar{U} + V_\chi}{V_\chi} + f_0$, with $f_0 \simeq 0.38$ [30] an *ad-hoc* parameter, introduced such that the front advances when $F > 0$ or recedes when $F < 0$. Fig. 1 a) displays the normalized front velocity, $v = V_f/V_\chi$ as function of the control parameter F . In the absence of the flow, corresponding to $F = 1 + f_0$, the reaction fronts are uniformly moving through the glass beads with a constant velocity $V_f = V_0 = 0.8V_\chi \pm 0.5 \mu\text{m/s}$ and exhibit a smooth shape [30]. On the contrary, when the flow is turned on, the front is distorted. Examples of the resulting front shapes with supportive ($F > 1.38$) and adverse flow ($F < 1.38$) are given in [30]. Depending on F , these fronts exhibit distinct self-affine scalings, quantified by the front width $w(\Delta x, t) \sim (\Delta x)^\alpha$, and the standard deviation of the temporal height fluctuations $w(x, \Delta t) \sim (\Delta t)^\beta$ [31].

We first consider a large flow rate where V_f is a linear function of F , see Fig. 1. For $|F| > 2.5$, the front propagates downstream, for both orientation of the mean flow Fig. 2(a) shows the width $w(\Delta x, t)$ of saturated fronts, i.e such that $\ell^*(t) \sim L$ [31], determined in several experiments realized at opposite mean-flow orientations. They display both similar roughnesses with $\alpha = 0.47 \pm 0.03$, and $\alpha = 0.53 \pm 0.04$, and growth exponents while $t^* \approx T$, with $\beta = 0.32 \pm 0.04$ and $\beta = 0.37 \pm 0.05$. As can be seen on Fig. 3 a), this suggests that for a large front velocity of either orientation, the front exhibits scale-invariant fluctuations with statistical properties consistent with the KPZ class, in agreement with the theoretical discussion around Eq. (3). In addition, since in the experiment $\bar{D} \sim V_f$ the expected KPZ noise $D \simeq \bar{D}/V_f$ is almost independent of V_f . This shows why the amplitude of $w(\Delta x, t)$ does not vary significantly with F for a given flow orientation [30], as can be seen in Fig. 2(a).

When $F \rightarrow 0$, some regions of the front pin to the flow

heterogeneities. In this configuration, the front propagates mainly upstream, from the bottom to the top of the cell, while locally the front exhibits transiently static regions, as can be seen in Fig. 4(a). Note that the moving parts exhibit a larger slope than the arrested or slowly propagating ones, which leads to a lateral growth of the fronts in this regime. When the opposite flow is amplified, the pinned portions become larger. The value F_{c+} for which the front eventually stops and remains static is $F_{c+} = 0.56 \pm 0.05$. Visible on Fig. 2 c) and d) for $F = 0.58$, $\alpha = 0.66 \pm 0.04$ and $\beta = 0.61 \pm 0.05$ are now consistent with the exponents of positive qKPZ model, $\alpha = \beta = 0.63$ (see [30] for additional measurements), and suggest here that the front undergoes a depinning transition when $F \rightarrow 0.56$.

Finally, when F decreases below F_{c+} , the transient front propagation becomes very short. For $F \approx 0$, the front is static almost instantaneously after the flow is turned on. When F becomes negative, the front propagates backwards, i.e. in the direction opposite to the chemical reaction. For sufficiently small F , $-2.22 \lesssim F \lesssim 0$, the front becomes static after a transient propagation and displays a particular sawtooth pattern [8]. One notes in Fig. 4(b) that the front is slowed down or arrested when it reaches a certain slope, resulting in the facet formation. Another depinning transition occurs at $F_{c-} \approx -2.22 \pm 0.05$, below which triangular static states become unstable and the front goes back to a phase moving from the top to the bottom of the cell.

As indicated in Fig. 3, these triangular shapes lead to a different roughness exponent of the transiently moving parts compared to the final static front as $F \rightarrow F_{c-}$ [30]. The roughness and growth exponents of propagating regions exhibit $0.62 \lesssim \alpha \lesssim 0.7$ and $0.63 \lesssim \beta \lesssim 0.69$, consistent with the observations in [25]. However, the final static fronts exhibit a larger roughness $0.73 \lesssim \alpha \lesssim 0.9$, which increases as the sawtooth slope rises when $F \rightarrow F_{c-}$. Interestingly, a crossover from $\beta \approx 0.65$ to $\beta \approx 0.33$ for larger scales is visible in Fig. 2(d), underlining the second depinning transition at F_{c-} . Close to F_{c-} , the front pins to point-like regions, while close to F_{c+} the pinning regions extend horizontally. This shows that receding fronts are consistent with negative qKPZ, known for similar pinning processes and interface morphologies [6, 24]. This model also predicts a first-order depinning transition, observed here as a jump in the $V_f(F)$ curve.

In order to better understand the behavior close to the transitions, we have performed lattice Boltzmann simulations in a 2D disordered porous medium (2048×2048 grid size) which solves the convection-diffusion-reaction and Darcy-Brinkman equations [2, 4, 30]. Fig. 1 b) displays the numerical front velocity versus $\hat{F} = (\bar{U} + V_\chi)/V_\chi + \hat{f}_0$, where hatted quantities denote parameters in the simulations with $\hat{f}_0 = 0.256$. Experiments and simulations are in good agreement. Two transitions occur at $\hat{F}_{c-} = -2.2 \pm 0.2$ and $\hat{F}_{c+} = 0.095 \pm 0.015$. While

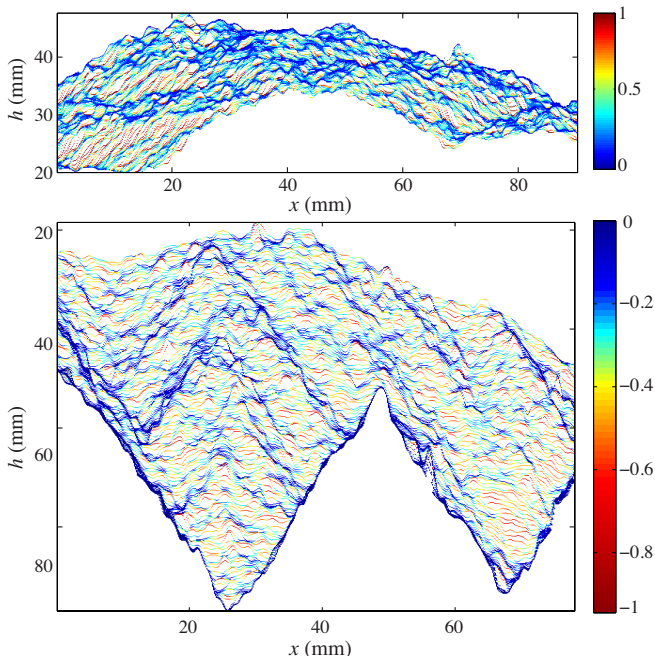


Figure 4: Successive experimental fronts at constant time intervals. Color represents local front velocity. Top: upward propagating front near F_c^+ ($F = 0.56$). Bottom: backward propagating front near F_c^- ($F = -1.24$).

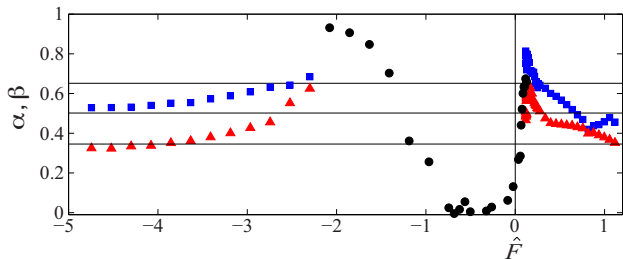


Figure 5: Roughness exponents in the simulations. Same symbols as in Fig. 3

the transition at \hat{F}_{c-} is very abrupt, the second one at \hat{F}_{c+} is more continuous. Moreover, the critical behavior can be fitted (Fig. 1.b, insert) with a power-law $V_f(\hat{F}) \sim (\hat{F} - \hat{F}_{c+})^{0.8 \pm 0.05}$, with an exponent slightly larger than the theory. This is consistent with a first-order transition at \hat{F}_{c-} and a second-order one at \hat{F}_{c+} . Below the first transition, $\hat{F} < \hat{F}_{c-}$, and beyond the second one, $\hat{F} > \hat{F}_{c+}$, the velocity $V_f(\hat{F})$ is almost linear in \hat{F} . Fig. 5 shows the roughness and growth exponents: for large $|\hat{F}|$, the scaling exponents of the numerics are in good agreement with experiments and the theory of the thermal KPZ class. Near the depinning transitions at \hat{F}_{c+} and \hat{F}_{c-} , the roughness exponents of the front $\alpha = 0.65 \pm 0.05$ and $\alpha = 0.9 \pm 0.05$ are consistent both with experiments and the positive and negative q-KPZ prediction respectively. The remaining differences in the

q-KPZ pinned phase are due to different initial conditions: In the experiment, the fronts propagate without flow (with their own roughness exponent at $\bar{U} = 0$) and then the flow is switched on, whereas in the simulation the initial front is almost flat (see [30] for details).

The good agreement between experiments, numerical simulations, and theory for the different KPZ universality classes can be understood through the *eikonal approximation*. For a thin front, the local front velocity follows the eikonal equation: $\vec{V}_f \cdot \vec{n} = V_\chi + D_m \kappa + \vec{U}(\vec{r}) \cdot \vec{n}$, where \vec{n} is the normal of the front, κ the curvature and $\vec{U}(\vec{r})$ the local flow velocity. Indeed, this equation is similar to the “flux-line model” of Kardar [12] where the chemical velocity plays the role of the Lorentz force, and the disordered flow that of the random force. After projection and neglecting higher-order terms [30], the eikonal approximation yields

$$\frac{\partial h}{\partial t} \simeq V_\chi \sqrt{1 + (\nabla h)^2} + \frac{D_m \nabla^2 h}{1 + (\nabla h)^2} + \bar{U} + \delta U_y(\vec{r}). \quad (4)$$

Assuming small gradients, and normalizing by V_χ , leads to equation (2) where $\bar{\eta} \equiv \delta U_y$ and with the parameters $\nu = l_\chi = D_m/V_\chi$, $\lambda = 1$, and $f = (\bar{U} + V_\chi)/V_\chi$, whose small renormalization due to the neglected terms can be estimated [34]. The difference $F - f = f_0$ is related to the space average of the KPZ term $f_0 \sim \frac{\lambda}{2} \langle (\nabla h)^2 \rangle_L$. Note that $\lambda = 1$ is independent of the front propagation direction, and fixed by the initial condition of the experiment. The reason why negative qKPZ describes the backward moving fronts, i.e. $\partial h / \partial t < 0$, can be understood by performing $h \rightarrow -h$, which is equivalent to measuring the front position along the $-\hat{y}$ axis, as discussed above. Finally, near the transition at F_{c-} , the slope of the sawtooths may be large. Although it correctly predicts the first-order transition, small-gradient qKPZ may not be quantitatively accurate. A more precise scenario for the transition has been proposed in [7], based on the PNG model [6] and extreme-value statistics [36].

In conclusion, chemical-wave propagation coupled with the disordered flow in a porous medium, can develop self-affine structures, with scaling exponents consistent with either KPZ or qKPZ classes. Remarkably, by tuning a single parameter, this system passes through three universality classes, providing a rich experimental setting to study growth phenomena. Slowly backward propagating fronts constitute beautiful experimental evidence of a chemical interface described by negative qKPZ. This opens the door for further investigations on frozen pattern formation in out of equilibrium systems [37]. Part of this phenomenology has been recently observed in magnetic domain walls [38]: it would be interesting to reach the thermal KPZ class there by increasing the driving.

This work was supported by Project Procathet RTRA Triangle de la Physique and PSL grant ANR-10-IDEX-0001-02-PSL.

-
- [1] M. A. C. Huergo, M. A. Pasquale, A. E. Bolzan, and A. J. Arvia, *Phys. Rev. E* **82**, 031903 (2010).
- [2] J. S. Langer, *Rev. Mod. Phys.* **52**, 1 (1980).
- [3] R. Messier and J. E. Yehoda, *J. Appl. Phys.* **58**, 3739 (1985).
- [4] J. Wakita, H. Itoh, T. Matsuyama, and M. Matsushita, *Journal of the Physical Society of Japan* **66**, 67 (1997).
- [5] D. Wilkinson and J. F. Willemsen, *J. Phys. A* **16**, 3365 (1983).
- [6] V. K. Horvath, F. Family, and T. Vicsek, *J. Phys. A* **24**, L25 (1991).
- [7] S. Santucci, R. Planet, K. J. Maloy, and J. Ortin, *EPL* **94**, 46005 (2011).
- [8] E. Bouchaud, *J. Phys.: Condens. Matter* **9**, 4319 (1997).
- [9] K. J. Maloy and J. Schmittbuhl, *Phys. Rev. Lett.* **87**, 105502 (2001).
- [8] S. Atis, S. Saha, H. Auradou, D. Salin, and L. Talon, *Phys. Rev. Lett.* **110**, 148301 (2013).
- [4] S. Saha, S. Atis, D. Salin, and L. Talon, *EPL* **101**, 38003 (2013).
- [5] L. A. N. Amaral, A. L. Barabasi, S. V. Buldyrev, S. T. Harrington, S. Havlin, R. Sadrlahijany, and H. E. Stanley, *Phys. Rev. E* **51**, 4655 (1995).
- [13] J. Maunuksela, M. Myllys, O. P. Kahkonen, J. Timonen, N. Provatas, M. J. Alava, and T. Ala-Nissila, *Phys. Rev. Lett.* **79**, 1515 (1997).
- [14] K. A. Takeuchi and M. Sano, *Phys. Rev. Lett.* **104**, 230601 (2010).
- [15] P. J. Yunker, M. A. Lohr, T. Still, A. Borodin, D. J. Durian, and A. G. Yodh, *Phys. Rev. Lett.* **110**, 035501 (2013). Comment by M. Nicoli, R. Cuerno, and M. Castro, *Phys. Rev. Lett.* **111**, 209602 (2013), and reply P. J. Yunker, M. A. Lohr, T. Still, A. Borodin, D. J. Durian, and A. G. Yodh, *Phys. Rev. Lett.* **111**, 209602 (2013).
- [16] K. A. Takeuchi, arXiv:1310.0220 (2014).
- [17] I. Corwin, arXiv:1106.1596 and references therein.
- [18] S. V. Buldyrev, A. L. Barabasi, F. Caserta, S. Havlin, H. E. Stanley, and T. Vicsek, *Phys. Rev. A* **45**, R8313 (1992).
- [19] M. Kardar, G. Parisi, and Y. C. Zhang, *Phys. Rev. Lett.* **56**, 889 (1986).
- [20] D. A. Kessler, H. Levine, and Y. Tu, *Phys. Rev. A* **43**, 4551 (1991).
- [21] H. Leschhorn et al., *Ann. Phys.* **6**, 1 (1997). For reviews see K. Wiese and P. Le Doussal, *Markov Processes Relat. Fields* **13** 777 (2007) and P. Le Doussal, *Int. Journal of Modern Physics B*, **24** (2010) 3855.
- [22] G. Parisi, *Europhysics Letters* **17**, 673 (1992).
- [23] L. H. Tang and H. Leschhorn, *Phys. Rev. A* **45**, R8309 (1992).
- [24] H. Jeong, B. Kahng and D. Kim, *Phys. Rev. Lett.* **77** 5094, (1996) and *Phys. Rev. E* **59** 047102, (1999).
- [25] Y. M. Choi, H. J. Kim, and I. Kim, *Phys. Rev. E* **66** 047102 (2002).
- [6] G. J. Szabo and M. J. Alava, *Physica A* **301**, 17 (2001).
- [27] A. Hanna, A. Saul, and K. Showalter, *J. Am. Chem. Soc.* **104**, 3838 (1982).
- [28] M. Leconte, J. Martin, N. Rakotomalala, D. Salin, *Phys. Rev. Lett.* **90**, 128302 (2003).
- [29] I. Bou Malham, N. Jarrige, J. Martin, N. Rakotomalala, L. Talon, and D. Salin, *J. Chem. Phys.* **133**, 244505 (2010).
- [30] Supplementary material to this article.
- [31] We define: $w(\Delta x, t) = \left\langle \sqrt{\langle [h(x, t) - \langle h \rangle_{\Delta x}]^2 \rangle_{\Delta x}} \right\rangle_L$ where $\langle \rangle_{\Delta x}$ represents an average over the length Δx , and $\langle \rangle_L$ a translational average along the front of length L . Temporal fluctuations are quantified by $w(x, \Delta t) = \left\langle \sqrt{\langle [h(x, t) - \langle h \rangle_{\Delta t}]^2 \rangle_{\Delta t}} \right\rangle_T$, where Δt is a time window, and T the duration of the experiment. Both quantities exhibit power laws, $w(\Delta x, t) \sim \Delta x^\alpha$ for $\Delta x \ll \ell^*(t)$, and $w(x, \Delta t) \sim \Delta t^\beta$ for $\Delta t \ll t^*(L)$, with $\ell^*(t)$ and $t^*(L)$ the spatial and temporal correlation lengths.
- [32] Talon, L., Martin, J., Rakotomalala, N., Salin, D. and Yortsos, Y. *Water Resour. Res.* **39**, 1135-1142 (2003).
- [33] M. Kardar, *Phys. Rep.* **301**, 85 (1998).
- [34] P. Le Doussal and K.J. Wiese, *Phys. Rev. E* **67**, 016121 (2003).
- [35] Gueudré, T., Dubey, A. K., Talon, L. and Rosso, *Phys. Rev. E* **89**, 041004 (2014).
- [36] Since pinning occurs where the flow field is slower than the chemical reaction, the transition results from the competition of two effects: (i) the probability to find a region of low flow velocity decreases as $F \rightarrow -\infty$ (ii) the “sawtooths” get sharper, increasing the probability to find new pinning points
- [37] V. Schaller et al. *PNAS* **108**, 19183 (2011). P. Le Doussal and T. Giamarchi, *Phys. Rev. B* **57** 11356 (1998).
- [38] K. W. Moon, D. H. Kim, S. C. Yoo, C. G. Cho, S. Hwang, B. Kahng, B. C. Min, K. H. Shin, and S. B. Choe, *Phys. Rev. Lett.* **110**, 107203 (2013).

Supplemental Material for Three universality classes for reaction fronts in disordered flows

1) Experimental and numerical details

a) Experimental statistics

Depending on the front mean velocity, different temporal resolutions between 200 and 2000 photos are recorded for each experiment. To enhance the statistics in the transient propagation regimes, for $-2.22 \lesssim F \lesssim 0.58$, we performed between 3 and 6 different realizations for each value of F . A total of 30 different values of F have been investigated, spanning from -6 to 8 .

b) Numerical methods

The heterogeneous permeability field $K(x, y)$ is generated according to a log-normal distribution, which is Gaussian correlated over a length l_K , as commonly assume to model groundwater flow [1]. The flow is computed by solving the Darcy-Brinkman equation:

$$\vec{0} = f_b \vec{e}_x - \frac{\mu}{K(x, y)} \vec{U}(x, y) + \mu \Delta \vec{U}(x, y), \quad (5)$$

where μ is the fluid viscosity and f_b is the body force driving the flow (*e.g.* buoyancy). The boundary conditions is periodic in the lateral direction. A convection-diffusion-reaction equation is then solved for the concentration (C) of the auto-catalytic reactant (iodide), normalized by the initial concentration of iodate:

$$\frac{\partial C}{\partial t} + \vec{U}(x, y) \cdot \vec{\nabla} C = D_m \Delta C + \tilde{\alpha} C^2 (1 - C), \quad (6)$$

where D_m and $\tilde{\alpha}$ are respectively the molecular diffusion and the reaction rate. Both equations are solved using Lattice Boltzmann schemes (see [2–4] for details). In the numerical study, the parameters $\tilde{\alpha}$ and D_m have been chosen to keep constant the ratio $l_\chi/l_K = \frac{\sqrt{2D_m}}{l_K \sqrt{\tilde{\alpha}}} = 0.126$, and the standard deviation of the log-normal distribution has been kept constant $\sigma_{lnK} = 0.5$. As in the experiments, the control parameter F is determined from the relative velocity between the reaction velocity V_χ and the mean flow velocity \bar{U} . The grid size is 2048×2048 and the computational cost is around 10 hours using 16 CPUs on a standard workstation.

For each value of F , around four different realizations is performed, and over 800 fronts are computed for each simulation. A total of hundred different values of F have been numerically generated, with thirty points close to the transition point at F_{c+} .

2) Experimental fronts aspects

In the absence of the flow, the reaction fronts are uniformly moving through the glass beads with a constant velocity $V_f = V_0 = 0.8V_\chi \pm 0.5 \mu\text{m/s}$. As can be seen on Fig. 6 center, if the interface is initially rough, it gradually relaxes towards a smooth front shape [see movie 1]. On the contrary, when the flow is turned on, the front is distorted. Examples of the resulting front shapes with supportive ($F > 1.38$) and adverse flow ($F < 1.38$) are shown on Fig. 6 left and right for high flow strength ($|F| \gtrsim 2.5$) [see movie 2 and 3].

3) Separation of the scalings between the static sawtooth shapes and the propagating regions of the fronts

The width of the front $w(\Delta x, t)$ is characterized by the standard deviation of the front height over a length scale Δx at a time t :

$$w(\Delta x, t) = \left\langle \sqrt{\langle [h(x, t) - \langle h \rangle_{\Delta x}]^2 \rangle_{\Delta x}} \right\rangle_L, \quad (7)$$

where $\langle \rangle_{\Delta x}$ represents an average over the length Δx , and $\langle \rangle_L$ a translational average along the front of length L . Temporal fluctuations are quantified by $w(x, \Delta t)$, corresponding to the standard deviation of the front height over a

time scale Δt at a given position x on the front:

$$w(x, \Delta t) = \left\langle \sqrt{\langle [h(x, t) - \langle h \rangle_{\Delta t}]^2 \rangle_{\Delta t}} \right\rangle_T, \quad (8)$$

where Δt is a time window, and T the duration of the experiment.

Both quantities exhibit power laws:

$$w(\Delta x, t) \sim \Delta x^\alpha \quad \text{for } \Delta x \ll \ell^*(t), \quad (9)$$

$$w(x, \Delta t) \sim \Delta t^\beta \quad \text{for } \Delta t \ll t^*(L), \quad (10)$$

with $\ell^*(t)$ and $t^*(L)$ the spatial and temporal correlation lengths.

In the negative qKPZ regime when F becomes close to F_{c-} , the front displays static sawtooth shapes at large scales, and one has to make a distinction between the scaling properties of the fronts before and after the formation of these patterns. Once the final static state is reached, the large scale sawtooth shape leads to a higher roughness exponent than the one determined during the transient propagation of the fronts, excluding these inclined static regions.

a) Experimental additional scalings

Figure 7 shows the roughness and growth exponents measured on the experimental fronts. In the blue region, corresponding to the pinned phase with negative F , the front exhibits a higher roughness exponent once the final static state is reached. Fig. 8 shows the corresponding $w(\Delta x, t)$ functions: left, determined from those sawtooth shape fronts, and center, during the transient propagation, excluding the inclined static regions under formation. The height temporal fluctuations determined during the transient regime for the same values of F are displayed on Fig. 9 left and center respectively.

When F becomes less negative, i.e. $F \gtrsim -1$, both the sawtooth size and inclination become smaller, and no more distinction is necessary between the scalings of the static state and the transiently moving state. For the positive qKPZ regime, one can note on Fig 8 right and 9 right, that the thermal KPZ exponents are recovered for $F = 0.64$.

For higher value of F , when $F \rightarrow 1 + f_0 = 1.38$, the mean flow velocity becomes nil and the noise is no more consistent enough to generate height fluctuations. This area corresponds to the hatched area on Fig. 7, and shows that the temporal fluctuations become uncorrelated: $\beta \rightarrow 0$, and the roughness of the front stays constant at $\alpha \simeq 0.8$.

b) Numerical additional scaling

As the two depinning transitions take place in the adverse flow regimes, only this configuration has been numerically investigated in this work. As can be seen on the Fig. 10, the numerical fronts scalings are quantitatively in good agreement with the experimental ones for both transitions points and at high values of \hat{F} . Similarly to the experimental fronts, the evolution of the roughness of the static front is quite more complex, and the same distinction between the static fronts and the moving fronts is necessary. As indicated on Fig.11, when $\hat{F} \rightarrow \hat{F}_{c-}$, the roughness of the static front $\alpha = 0.87 \pm 0.05$ becomes close to one and corresponds to the characteristic sawtooth shape.

Fig. 11 also shows the roughness of the front close to \hat{F}_{c+} , with the value $\alpha = 0.68 \pm 0.05$ in agreement with the positive qKPZ equation. In this regime, it is interesting to note that there is a discrepancy on Fig. 10, between the

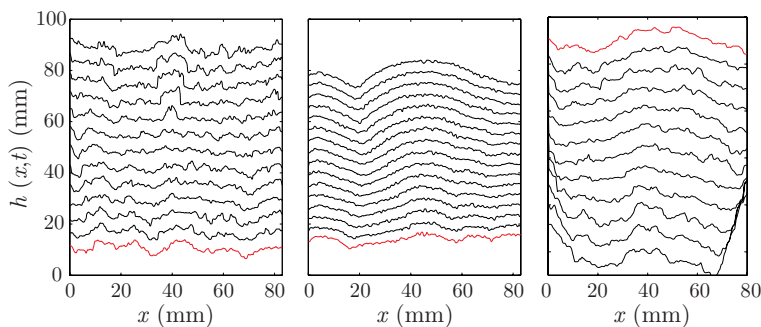


Figure 6: Successive experimental fronts at constant time intervals (red: starting front). Left: $F = 6.01$, upward front propagation with supportive flow. Center: $F = 1.38$: relaxation pattern in the absence of flow. Right: $F = -2.66$, backward propagating front in adverse flow.

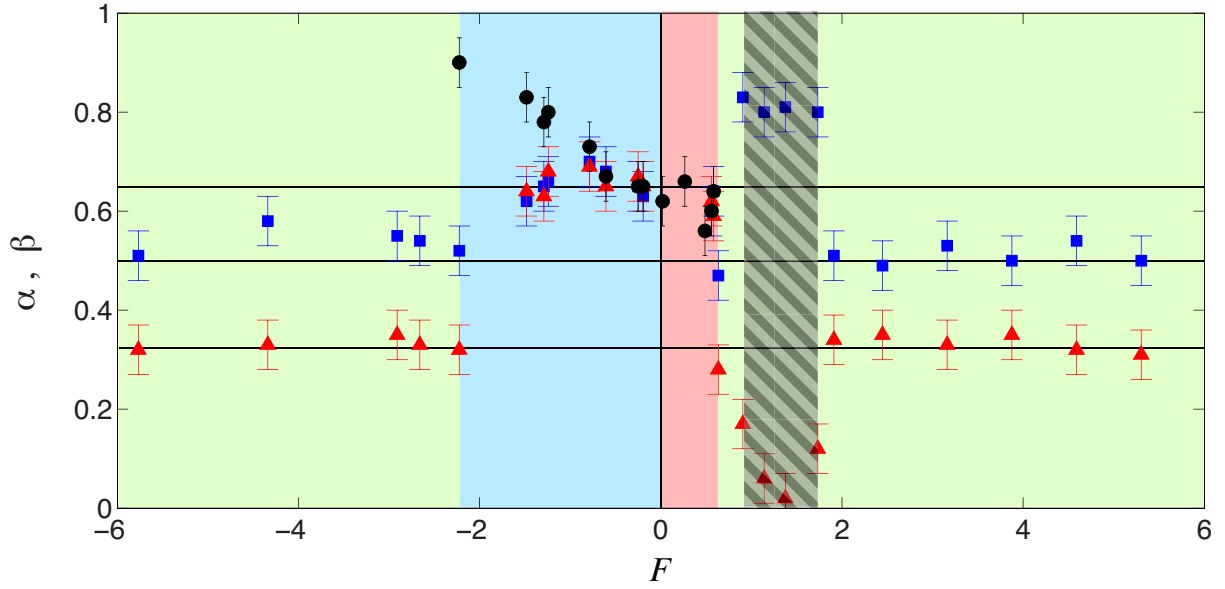


Figure 7: Roughness exponent α for moving fronts (blue squares), roughness in the pinned phase (black circles) and growth exponent β (red triangles); versus F in the experiments. Hatched area corresponds to weak noise region when $\bar{U} \rightarrow 0$. Green region: moving phase, blue region: negative qKPZ configuration ($F < 0$ and $V_\chi > 0$), and red region: positive qKPZ configuration ($F > 0$ and $V_\chi > 0$).

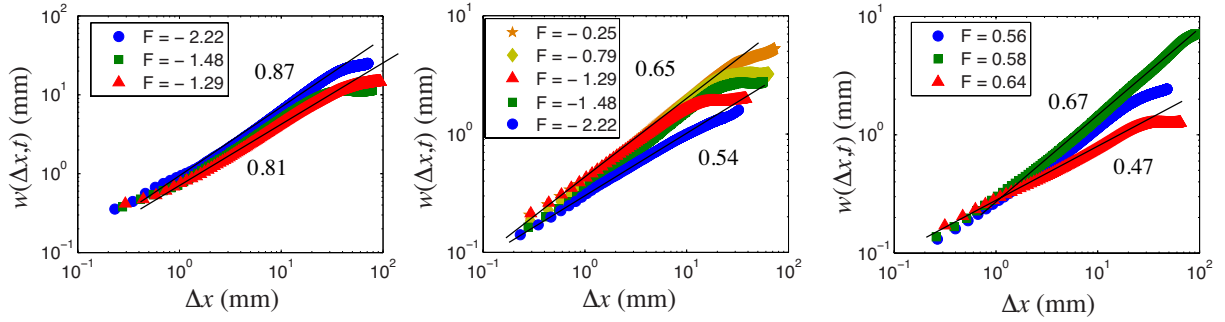


Figure 8: Left and center: roughness of the fronts in the negative qKPZ regime. Left: determined for the final sawtooth static fronts, center: determined during the transient propagation and excluding the frozen portions of the front. Right: roughness of the fronts in the positive qKPZ regime for upstream propagating fronts.

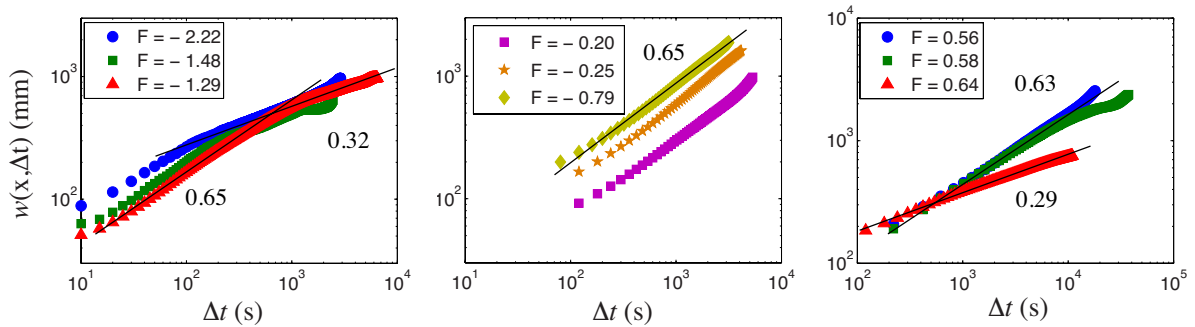


Figure 9: Temporal fluctuations in the qKPZ regime determined during the transient propagation of the front. Left: close to F_{c-} excluding the sawtooth shape frozen portions, center: for intermediate values of negative F , and right: close to F_{c+} .

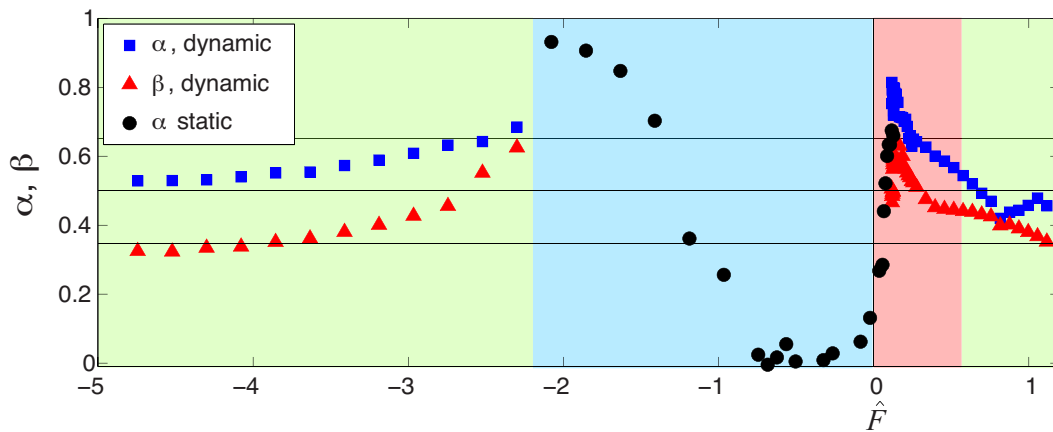


Figure 10: Roughness exponent α for moving fronts (blue squares), roughness in the pinned phase (black circles) and growth exponent β (red triangles); versus \hat{F} in the simulations. Green region: moving phase, blue region: negative qKPZ configuration ($\hat{F} < 0$ and $V_\chi > 0$), and red region: positive qKPZ configuration ($\hat{F} > 0$ and $V_\chi > 0$).

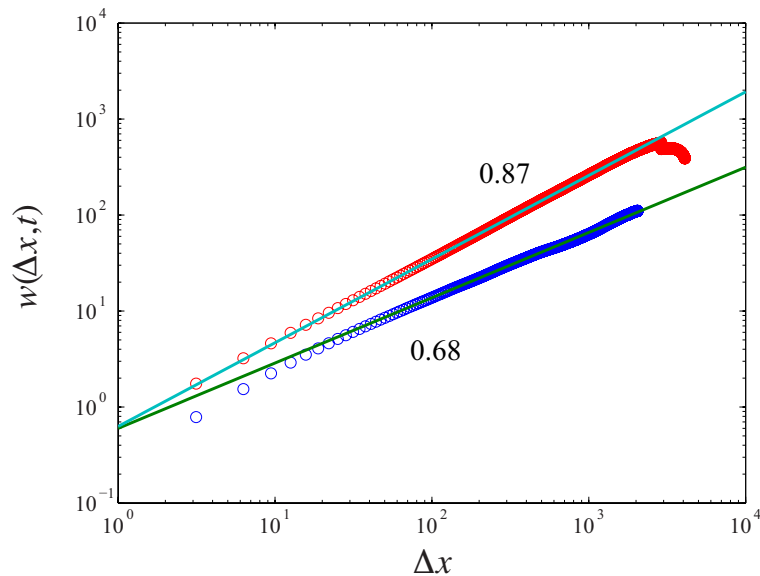


Figure 11: Numerical front roughness of the final static fronts at $\hat{F} \simeq \hat{F}_{c+}$, blue, and $\hat{F} \simeq \hat{F}_{c-}$, red.

roughness measured in the moving regime ($\alpha = 0.75 \pm 0.05$) and the one measured in the static regime, which should be compared to the Directed Percolation (as notified by Amaral *et al.* [5]).

Far from the two transitions when $\hat{F} < \hat{F}_{c-}$ or $\hat{F} > \hat{F}_{c+}$, the two exponents become quite close to the “thermal” KPZ ones. Indeed one have at $\hat{F} = -6$, $\alpha = 0.55 \pm 0.05$ and $\beta = 0.32 \pm 0.05$ and at $\hat{F} = 1$, one have : $\alpha = 0.45 \pm 0.05$ and $\beta = 0.32 \pm 0.05$.

3) Region of low F

As \hat{F} is decreased further on Fig. 10, the roughness of the numerical fronts drops to zero at $\hat{F} \simeq -0.5$ and then increases again as F approaches the second transition at \hat{F}_{c-} . We can note here that, deep inside the pinned phase, we expect the final front’s shape to depend on the initial conditions. Both in the experiments and numerics, when $\hat{F} \rightarrow 0$, the front moves only by a small amount before getting pinned. In fact, it is worth noting that the Poisson point disorder models (first layer PNG as in [6] or in a more realistic form in [7]) predict that the final, pinned configuration, will have the same roughness as the initial one. Hence in the numerics, it is expected that the roughness drop to zero as the initial conditions is flat, whereas in the experiments the initial fronts are never perfectly

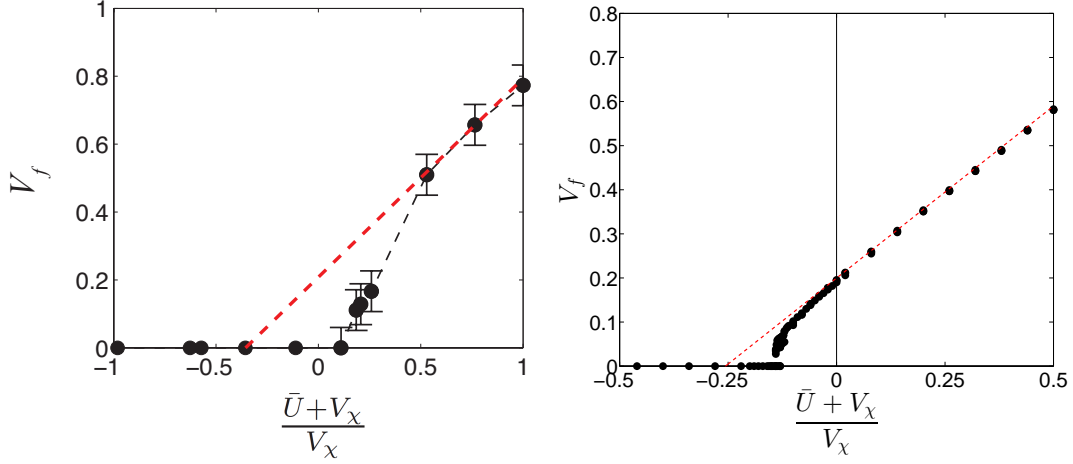


Figure 12: Front mean velocity versus the relative mean flow rate: $(\bar{U} + V_\chi)/V_\chi$. Dashed red lines indicate the linear fit with the right moving branch and its intersection with the x axis determines the value of f_0 . Left: $f_0 = 0.38$ in experiments, and right: $f_0 = 0.256$ in simulations.

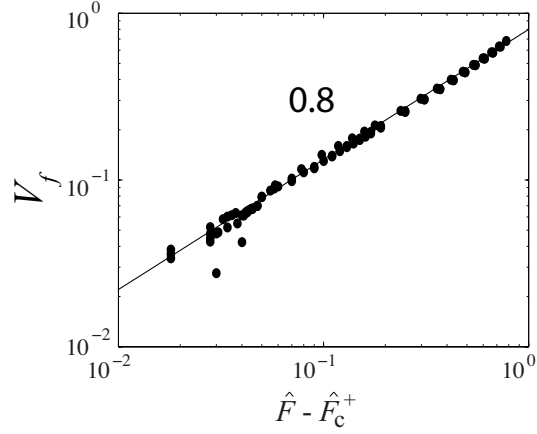


Figure 13: Numerical front velocity versus $\hat{F} - \hat{F}_{c+}$.

flat as they have already travel through the glass beads before the flow is switched on. When we get closer to \hat{F}_{c-} , the front moves for longer distance before getting pinned, and thus recover a more universal behavior as $\hat{F} \rightarrow \hat{F}_{c-}$.

4) Control parameter definition

As a control parameter, we define $F = \frac{\bar{U} + V_\chi}{V_\chi} + f_0$ in the experiments and $\hat{F} = \frac{\bar{U} + V_\chi}{V_\chi} + \hat{f}_0$ in the simulations. One can note that, in the porous medium, it is quite unclear if one should use V_χ or $V_0 = 0.8V_\chi \pm 0.5\mu\text{m/s}$ (*i.e.* including or not the effect of tortuosity/porosity) to determine F . Here, we are using V_χ to define F as for the eikonal approximation. Indeed, this parameter V_χ has shown to lead to the right estimation of the sawtooths angle when the fronts are static [8]. In the simulations however, porosity and tortuosity are both equal to one, the problem is then not present as $V_0 = V_\chi$.

By analogy with the qKPZ behaviour, the constant f_0 is determined by fitting the right velocity branch far from its pinning threshold (see Figs. 12). As described below, we attribute this constant value to the average roughness of the front. A closer inspection of the Fig. 12 right, shows that it can be fitted with a power-law $V_f(\hat{F}) \sim (\hat{F} - \hat{F}_{c+})^{0.8 \pm 0.05}$, with $\hat{F}_{c+} \simeq 0.095 \pm 0.015$ as shown on Fig. 13. One can note that, the value $F = 1 + f_0$ is quite singular since then the noise is nil, but not the driving force.

In the numerics, below the first transition, $\hat{F} < \hat{F}_{c-}$, and beyond the second one, $\hat{F} > \hat{F}_{c+}$, the velocity $V_f(\hat{F})$ is almost linear with $V_f = 0.9\hat{F} + 0.52$ and $V_f = 0.8\hat{F}$, respectively. Both branches have different slopes and differ

from the prediction of the KPZ equation ($v/f \sim 1$ at large f). Similarly, in the experiments, we note that both negative $F < F_{c-}$ and positive $F_{c+} < F < 1.38$ linear branches have a different slope than one: $V_f = 0.55F - 0.15$ and $V_f = 0.56F$ respectively. In addition, for the supportive flow regime in the experiments, this slope becomes $V_f = 1.12F - 0.85$. We attribute this behavior to a nonlinear interaction between the chemical reaction and the flow field, which enhances mixing and front velocity as studied in [9–11]. Indeed, since flow heterogeneities necessarily enhanced the mixing and thus the reaction rate, one can expect at first order in $\epsilon = \bar{U}/v_\chi$ to have an effective chemical velocity: $V_\chi \rightarrow V_\chi(1 + a|\epsilon|)$ leading to an average front velocity $V_f = (1 - a)\bar{U} + V_\chi$ for adverse flow ($\epsilon < 0$) and $V_f = (1 + a)\bar{U} + V_\chi$ for supportive flow ($\epsilon > 0$).

5) From the eikonal approximation to the qKPZ equation

For a thin front, the local front velocity follows the eikonal equation:

$$\vec{V}_f \cdot \vec{n} = V_\chi + D_m \kappa + \vec{U}(\vec{r}) \cdot \vec{n}, \quad (11)$$

where \vec{n} is the normal of the front, κ the curvature and $\vec{U}(\vec{r})$ the local flow velocity. Indeed, this equation is similar to the “flux-line model” of Kardar [12] where the chemical velocity plays the role of the Lorentz force and the disordered flow of the random force. After projection the eikonal approximation yields to:

$$\frac{\partial h}{\partial t} = \sqrt{1 + s^2} \left[D_m \partial_x^2 h / (1 + s^2)^{3/2} + V_\chi + (\bar{U} + \delta U_y(\vec{r}) - s \delta U_x(\vec{r})) / \sqrt{1 + s^2} \right],$$

with $s = \nabla h$ and $\vec{U}(\vec{r}) = \bar{U} \vec{e}_y + \delta \vec{U}(\vec{r})$,

which, considering that the flow is highly anisotropic $\delta U_x \ll \delta U_y$, gives:

$$\frac{\partial h}{\partial t} \simeq \frac{D_m \nabla^2 h}{1 + (\nabla h)^2} + V_\chi \sqrt{1 + (\nabla h)^2} + \bar{U} + \delta U_y(\vec{r}). \quad (12)$$

Finally, assuming small gradients and neglecting higher order terms, leads to the qKPZ equation:

$$\frac{\partial h}{\partial t} \simeq D_m \nabla^2 h + \frac{V_\chi}{2} (\nabla h)^2 + \delta U_y(\vec{r}) + \bar{U} + V_\chi. \quad (13)$$

After normalizing by V_χ , we can write the qKPZ equation with the following parameters:

$$\begin{aligned} \nu &= l_\chi = D_m / V_\chi \\ \lambda &= 1 \\ \bar{\eta} &\equiv \delta U_y \\ f &= \frac{\bar{U} + V_\chi}{V_\chi}, \end{aligned}$$

6) Disorder measurements

In the experiment $\bar{D} \sim V_f$ and V_f is proportional to F for large mean flow velocities, i.e. $|F| > 2.5$. The expected KPZ noise $D \simeq \bar{D}/V_f \sim \bar{D}/F$ becomes then almost independent F . \bar{D} can be deduced experimentally from the flow local velocity fluctuations. The width $\sigma(F) \sim \bar{D}$ of the corresponding flow velocity PDF, at a given value of F , can be estimated with tracer transport experiments [8]. Fig. 14 a) shows the value of $\sigma(F)$ determined from tracer front dispersion experiments, and show that σ is proportional to F for both signs of F and $|F| > 2$. The dependence of σ/F with F is shown on Fig. 14 b). One can note that, $\sigma/F \sim \bar{D}/F \simeq cste$ for $F > 2$, with a different value depending on the the sign of F .

Supplemental movie 1

Reaction front propagation in the absence of flow, i.e. at $F = 1 + f_0 = 1.38$.

http://www.fast.u-psud.fr/~atis/Movie1_Q0.avi

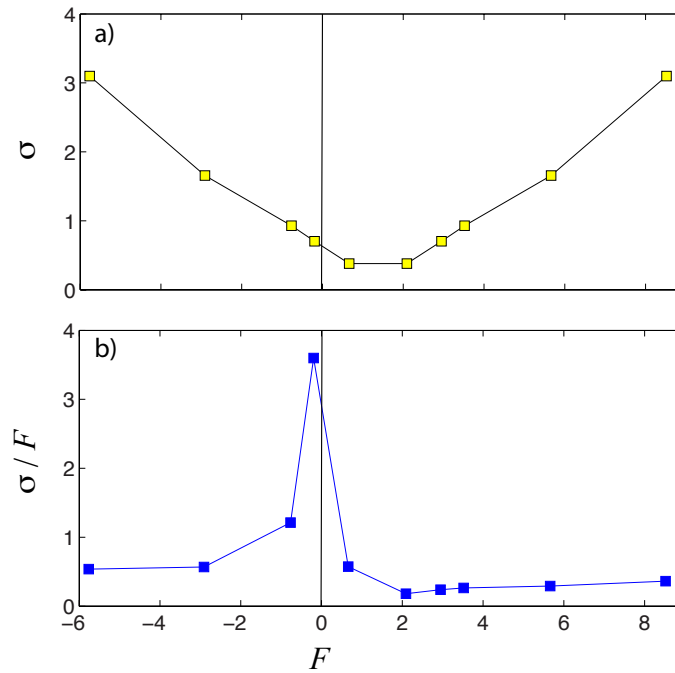


Figure 14: a) The dependence to F of the width σ of the flow velocity fluctuations PDF determined from tracer transport experiments. b) $\sigma/F \sim \bar{D}/F \simeq D$, the estimated KPZ noise dependence on F .

Supplemental movie 2

Upward propagating reaction front at large flow rate, for positive mean flow orientation at $F = 3.16$. In this configuration both the chemical wave velocity and the mean flow velocity are oriented toward the top.
http://www.fast.u-psud.fr/~atis/Movie2_Q025_up.avi

Supplemental movie 3

Downward propagating reaction front at large flow rate, for negative mean flow orientation at $F = -4.34$. In this configuration the chemical wave velocity is oriented toward the top and the mean flow velocity toward the bottom.
http://www.fast.u-psud.fr/~atis/Movie3_Q08_down.avi

Supplemental movie 4

Upward propagating reaction front at low flow rate, for negative mean flow orientation at $F = 0.58$. In this configuration the chemical wave velocity is oriented toward the top and the mean flow velocity toward the bottom.
http://www.fast.u-psud.fr/~atis/Movie4_Q011_down.avi

Supplemental movie 5

Downward propagating reaction front at low flow rate, for negative mean flow orientation at $F = -1.25$. In this configuration the chemical wave velocity is oriented toward the top and the mean flow velocity toward the bottom.
http://www.fast.u-psud.fr/~atis/Movie5_20_down_SSB.avi

[1] G. Matheron, *Éléments pour une théorie des milieux poreux*, Masson, Paris (1967). G. Dagan, *Water Resour. Res.* **18**, 813-833 (1982). L. Gelhar and C. Axness, *Water Resour. Res.* **19**, 161-180 (1983).

- [2] Talon, L., Martin, J., Rakotomalala, N., Salin, D. and Yortsos, Y. *Water Resour. Res.* **39**, 1135-1142 (2003).
 - [3] I. Ginzburg, *Phys. Rev. E* **77**, 066704 (2008).
 - [4] S. Saha, S. Atis, D. Salin, and L. Talon, *EPL* **101**, 38003 (2013).
 - [5] L. A. N. Amaral, A. L. Barabasi, S. V. Buldyrev, S. T. Harrington, S. Havlin, R. Sadrlahijany, and H. E. Stanley, *Phys. Rev. E* **51**, 4655 (1995).
 - [6] G. J. Szabo and M. J. Alava, *Physica A* **301**, 17 (2001).
 - [7] Gueudré, T., Dubey, A. K., Talon, L. and Rosso, *Phys. Rev. E* **89**, 041004 (2014).
 - [8] S. Atis, S. Saha, H. Auradou, D. Salin, and L. Talon, *Phys. Rev. Lett.* **110**, 148301 (2013).
 - [9] J. Xin, *SIAM Review* **42**, 161-230 (2000).
 - [10] B.F. Edwards, *Phys. Rev. Lett.* **89**, 104501 (2002).
 - [11] B. F. Edwards, *Chaos* **16**, 043106 (pages 8) (2006).
 - [12] M. Kardar, *Phys. Rep.* **301**, 85 (1998).
-